The Astronomical Journal, 171:217 (12pp), 2026 April https://doi.org/10.3847/1538-3881/ae3f9d

Interstellar Ultraviolet Lyα High Resolution Mapping from the New Horizons P-Alice Instrument

Tracy M. Becker[1,2], G. Randall Gladstone[1,2], Joel Wm. Parker[3], J. Michael Shull[4,5], Seth Redfield[6], Sarah Ruetschle[2,7], Nathaniel J. Cunningham[8], Cynthia S. Froning[1], Joshua A. Kammer[1], John R. Spencer[3], Marc Postman[9], Tod R. Lauer[10], Jayant Murthy[11], Maarten H. Versteeg[1], Jon P. Pineau[12], Kurt D. Retherford[1,2], Anne J. Verbiscer[13], Pontus C. Brandt[14], Kelsi N. Singer[3], and S. Alan Stern[3]
[1] Southwest Research Institute, 6220 Culebra Road, San Antonio, TX 78238, USA
[2] University of Texas San Antonio, 1 UTSA Circle, San Antonio, TX 78249, USA
[3] Southwest Research Institute, 1301 Walnut Street Suite 400, Boulder, CO 80302, USA
[4] Department of Astrophysical & Planetary Sciences, CASA University of Colorado, Boulder, CO 80309, USA
[5] Department of Physics & Astronomy, University of North Carolina Chapel Hill, NC 27599, USA
[6] Astronomy Department and Van Vleck Observatory, Wesleyan University, Middletown, CT 06459, USA
[7] John Carroll University, 1 John Carroll Boulevard, University Heights, OH 44118, USA
[8] Nebraska Wesleyan University, 5000 Saint Paul Avenue, Lincoln, NE 68504, USA
[9] Space Telescope Science Institute, 3700 San Martin Drive, Baltimore, MD 21218, USA
[10] NOIRLab, P.O. Box 26732, Tucson, AZ 85726, USA
[11] Indian Institute of Astrophysics, Bengaluru 560 034, India
[12] Stellar Solutions, Stellar Solutions Aurora, CO 80011, USA
[13] Department of Astronomy, University of Virginia, Charlottesville, VA 22904, USA
[14] The Johns Hopkins University Applied Physics Laboratory, 11100 Johns Hopkins Road, Laurel, MD 20723, USA
Received 2025 November 12; revised 2026 January 27; accepted 2026 January 28; published 2026 March 10

Abstract

We present New Horizons Alice spectral observations of interstellar hydrogen Lyα emissions at a vantage point of 57 au from the Sun. The observations were conducted as a pair of orthogonal scans to produce high spatial angular resolution measurements of a dark patch of sky located at high Galactic latitudes. We find that the brightness of the UV background remains relatively constant over the selected sky region, with the exception of areas near a few bright stars and galaxies. Most stars do not affect the brightness of Lyα in this region; however, we detect a 25 Rayleigh Lyα enhancement near the location of hot subdwarf CD-38 222. This enhancement is consistent with nebular emission produced by ionizing photons from a bow shock as the object interacts with a high-latitude interstellar gas cloud. We do not find correlations of Lyα or background UV brightness with dust structures seen by the Planck space observatory. Our analysis at higher angular resolution and with the full Alice bandpass of 520–1870 Å confirms the results of the global Lyα maps produced by G. R. Gladstone et al. at lower spatial resolution. The near-constant Lyα is consistent with their interpretation that scattering of H within our Local Bubble produces a nearly isotropic Lyα distribution. Future Alice global scans in photometer mode can be used to assess changes in the Lyα sky as a function of solar distance. High-resolution FUV Lyα scans with the full spatial and spectral information should be repeated over the entire sky to resolve additional small-scale structures.

Unified Astronomy Thesaurus concepts: H I line emission (690); Ultraviolet spectroscopy (2284); Interstellar medium (847); Stellar bow shocks (1586)

1. Introduction

At a distance of 56.7 au from the Sun, the New Horizons spacecraft was uniquely situated to study the interstellar distribution of hydrogen Lyα emissions at ultraviolet (UV) wavelengths without the significant resonant backscattering of solar Lyα that obscures such observations from Earth. Lyα emissions are produced at a wavelength of 1215.67 Å when the electron in hydrogen (H) atoms transitions from the $n = 2$p orbital state to the $n = 1$ s ground state. Because hydrogen is the most abundant atom in the Universe, the Alice UV spectrograph instrument on board New Horizons (P-Alice) observed a background of Lyα emission both within the interplanetary medium (IPM) and from sources in the local interstellar medium (LISM). The Lyα background within the inner solar system is dominated by solar light backscattered by neutral hydrogen atoms across the IPM and in the H-dense clouds escaping from planets, known as planetary coronae (R. R. Meier et al. 1977; R. R. Meier 1991), making Earth-based interstellar Lyα emission observations a challenge.

G. R. Gladstone et al. (2025) produced the first all-sky Lyα map from a heliocentric distance >50 au using UV observations acquired in 2023 from the Alice UV spectrograph on board the New Horizons spacecraft (S. A. Stern et al. 2008). The all-sky UV data were acquired in a photon-counting (photometer) mode while the spacecraft conducted 75 great circles, each contiguously spaced 2° apart until nearly the entire sky had been covered. In this photometer mode, all photons across the Alice bandpass are collected but no spatial information along the instrument FOV or spectral information is recorded for those photons. In addition to previously acquired great circles on the sky observed by the Alice

instrument at distances 7.624 au, 11.337 au, 16.991 au, 32.679 au, 32.919 au, 37.561 au, and 43.775 au, G. R. Gladstone et al. (2021) found that approximately half of the observed Lyα signal beyond Pluto's distance can be attributed to solar light backscattered by interstellar H atoms passing through the outer solar system. The remaining nearly isotropic ~50 Rayleigh (R) background is likely produced by a recombination of H atoms in the wall of the Local Bubble of hot gas surrounding the solar system that are ionized by very young, bright stars. G. R. Gladstone et al. (2025) did not find any strong, large-scale correlations with nearby cloud structures of the LISM (S. Redfield 2009; S. Redfield & J. L. Linsky 2015) or with expected structures of the heliosphere, such as the hydrogen wall associated with the heliopause and the galactic plane (R. Lallement et al. 2011).

The focus of this work is the analysis of two additional 2023 Lyα Alice observations obtained while pointing in a relatively dark (fewer UV-bright stars) $4° \times 4°$ region of the sky near the Galactic south pole, centered near R.A. $\sim 10°$, decl. $\sim -38°$, or in Galactic coordinates (l, b) $\sim(315°, -78°)$. These observations were conducted as a pair of orthogonal scans that would result in a much higher spatial resolution of $\sim 0.^{\circ}2$ to assess finer structure in Lyα, and therefore the distribution of H. These observations recorded the full spectral bandpass for each Alice row during each observation rather than operating in a photometer mode, enabling the analysis of the UV spectrum and the ability to isolate Lyα and other key wavelength regions of interest. The longer (900 s) integrations also enabled a more sensitive search for variability. These observations can be used to validate the assumption for the global all-sky maps (G. R. Gladstone et al. 2025) that the photons detected by the sensor were dominated by the Lyα emissions.

In this work, we present the results from the high-resolution Lyα spectral mapping scans. In Section 2, we describe how the observations were acquired, and in Section 3 we describe the data processing. In Section 4, we compare our results with the all-sky Lyα maps produced by G. R. Gladstone et al. (2025) and look for correlations in structure with UV maps produced by the Galaxy Evolution Explorer (GALEX) space observatory (D. C. Martin et al. 2005; P. Morrissey et al. 2005) and structures observed in longer-wavelength maps produced by the European Space Agency's Planck mission (e.g., Planck Collaboration et al. 2011). We summarize our conclusions in Section 5.

2. New Horizons Alice Observations

The slews were designed to step the $0.^{\circ}1$ wide Alice slot one slot-width in the along-track direction for the duration of a 900 s data acquisition. The acquisitions were done in histogram mode, which creates a single time-integrated image. This conserved data volume was compared with the pixel-list mode, which records the time and detector position of every individual detection event. Each single acquisition covered $\sim 0.^{\circ}2$ of sky, with an approximate scan rate of ~ 0.0002 deg s^{-1}. Each scan was comprised of 40 acquisitions, with each subsequent acquisition starting immediately after the end of the previous acquisition, resulting in $\sim 0.^{\circ}1$ of overlap and $\sim 0.^{\circ}1$ of new sky coverage with each time step within the slot. The much larger 2° wide box has much more repeat coverage with each time step. The Alice field of view (FOV) was first slewed in decreasing decl. The spacecraft was rotated

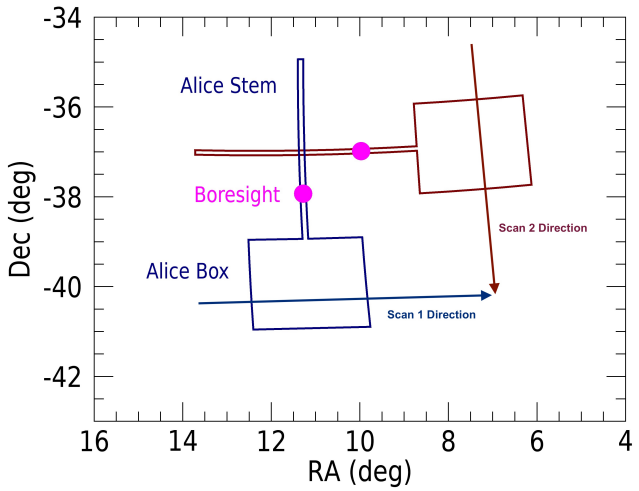

Figure 1. Visualization of the New Horizons Alice slit orientation at two times during the high-resolution Lyα scans. The spacecraft was slewed perpendicular to the slit first in decl., and then the slit was rotated to slew in R.A. for the narrow slot (stem) to cover the same $4° \times 4°$ region.

90° and the FOV was repositioned to slew in decreasing R.A. such that the observed regions overlapped (see Figure 1).

As described in more detail by S. A. Stern et al. (2008), during each acquisition light enters the 40 mm × 40 mm entrance aperture and is focused by an $f/3$ off-axis paraboloidal primary mirror through the entrance slit, where the light then falls on a diffraction grating that disperses the light onto a double-delay line two-dimensional microchannel plate (MCP) detector (O. H. W. Siegmund et al. 1993). The full detector consists of 32 spatial elements or rows, 21 of which are within the optically active area of the detector where data are collected. Each row has a spatial height of $0.^{\circ}29$ and a spatial width of $0.^{\circ}1$ for the 13 rows in the slot or a spatial width of $2.^{\circ}0$ for the eight rows in the box. The spectrograph has a bandpass from 520 Å to 1870 Å and a filled-slit spectral resolution of 9 Å near the center of the instrument slot. Details related to the detector's response as a function of wavelength and our spectral calibration are described in Section 3.

3. Data Processing and Analysis

The observations were calibrated by applying standard Alice data reduction techniques, which were described in greater detail by S. A. Stern et al. (2008) and A. J. Steffl et al. (2020). These include a dead-time correction, a stim pixel correction, a dark subtraction, and the application of the effective area. The dead-time correction is needed to account for the finite time (~ 18 μs) during which the detector processed detected counts and was insensitive to new counts. The stim pixel correction corrects for any shifting in which the photon counts are mapped to the physical Alice detector due to temperature changes. To remove counts introduced by the detector itself, we subtract a dark counts image from the data. We use the dark image pa_dark_003a.fit which was acquired in 2019 August 31, by integrating with the Alice aperture door closed for 10,800 s, resulting in a dark count rate on the order of 125 Hz that was then scaled to the integration time of our observations. The Alice pipeline applies an effective area as a function of wavelength to adjust for the detector's sensitivity across the Alice bandpass; the effective area is based on frequent observations of calibration stars (typically ρ Leo).

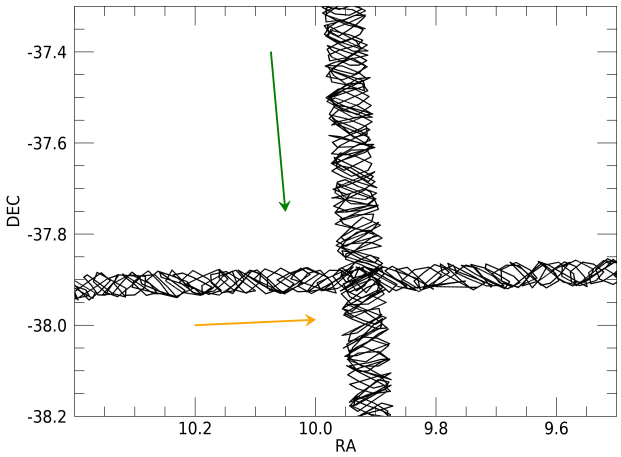

Figure 2. The position of the Alice FOV boresight at a 1 s interval cadence (black dots) shows that the jitter of the spacecraft pointing was on the order of $0.^{\circ}1$. The arrows point in the direction of motion of the spacecraft slew. The magnitude of the jitter is within the PSF of the detector and therefore does not introduce additional errors in how we map the high spatial resolution measurements of Lyα.

3.1. Spacecraft Pointing

Jitter in the spacecraft pointing during the Alice observation could impact the interpretation of the spatial distribution of the measured brightness signal. The jitter results from thruster firings on New Horizons to maintain pointing and slewing within a programmed limit cycle (deadband) for the observation. Figure 2 shows that the performance of the spacecraft pointing was very good, with across-track jitter on the order of $0.^{\circ}1$, well within the $0.^{\circ}27$ extent of each spatial pixel along the slit. Jitter along-track was of a similar magnitude and is within the point-spread function (PSF) of the observations. Therefore, no additional corrective actions were taken to account for spacecraft jitter.

3.2. Spectra in the Alice Box

An example of the reduced spectra from two rows acquired during the same observation on 2023-08-22T12:26:52.798 are shown in Figure 3. The purple spectrum is from detector Row 16 (zero-indexed) illuminated by the narrow slot portion of the Alice slit, and the orange spectrum is from detector Row 23 that is illuminated by a much wider box portion of the Alice slit. The differences between these spectra are due to the design of the detector: in order to avoid saturation by solar Lyα during observations, the detector region of the MCP near Lyα was left bare while the photocathode at shorter wavelengths (520 Å–1180 Å) is coated with KBr and the photocathode at longer wavelengths (1250 Å–1870 Å) is coated with CsI to enhance signal sensitivity outside the Lyα spectral region (S. A. Stern et al. 2008). Diffuse Lyα emissions filling the much narrower slot fall entirely within the bare, uncoated portion of the detector, resulting in a narrow, symmetric Gaussian shape of the Lyα peak, though at a reduced brightness. Diffuse Lyα emissions filling the much wider box, however, fall across a broader region on the detector, including the sensitive photocathodes on either side of the bare detector region (G. R. Gladstone et al. 2021). The measured effective area of the detector applied during the data reduction pipeline process corrects for the difference in sensitivity of the bare detector region between 1180 Å and

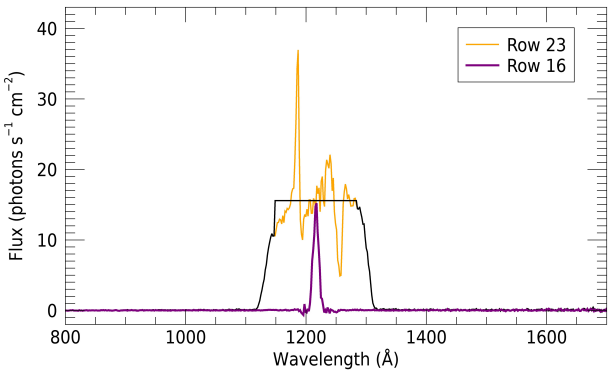

Figure 3. Lyα photons that enter through the Alice slit fall on the bare region of the detector, producing the observed narrow, symmetric Gaussian emission line near 1216.1 Å, as seen in Row 16 (purple). The larger aperture of the Alice box results in off-axis Lyα photons reaching the detector across a broader range of wavelengths, including those on the more sensitive KBr and CsI coatings on either side of the bare detector. The pipeline application of the effective area accounts for the differences in sensitivity across these three detector regions; however, artificial spikes in signal are produced at the transitions of those regions, as seen in the spectra of Row 23 (orange). We correct for the spikes by finding the average signal in the region and using that value across the region (black). As described in the text, total Lyα signal collected in rows within the Alice box are then normalized to the observed signal in Row 16.

1250 Å. However, the sharp boundary transition between the bare detector region and the coated photocathodes results in the artificial spikes in the signal when the effective area is applied.

To correct for these artificial spikes seen in Figure 3, we find the average of the signal between the spectral region 1148.7 Å and 1283.7 Å and apply that mean value across the same spectral range. This technique produces an average signal that is close to the value observed near 1211 Å in the box, which should be the most accurate possible value of the observation. The intensity of the Lyα emission is then scaled to the Lyα brightness at the boresight in Row 16 (Section 3.3), which has been extensively calibrated.

3.3. Row-to-Row Sensitivity Calibration

The full width at half-maximum spectral resolution of the filled slit is 9 Å. We observed that the Lyα signal, centered at 1216 Å, is broadened instrumentally by $\pm$18 Å. Therefore, when calculating the total brightness of Lyα in any of the rows along the slot, we sum the signal between 1201 Å and 1231 Å to capture all of the Lyα signal. In the Alice box, we sum the signal between 1116 Å and 1316 Å for similar instrumental reasons.

Although the standard pipeline accounts for wavelength-dependent variations of the detector's sensitivity, it does not correct for sensitivity differences in the spatial dimension. We correct for row-to-row variations by analyzing the Alice dataset "ali_0554925098_0x4b2," also acquired in 2023, that was designed as a 3600 s integration in a dark region of the sky to sensitively measure the cosmic UV background (CUVB); see J. Murthy et al. (2025). Since our primary focus in this work is at Lyα wavelengths, we total the Lyα counts in each row of the CUVB data and normalize them to the signal observed in Row 16 (zero-indexed; Figure 4). Row 16 is considered the boresight for the Alice airglow and has been extensively calibrated over the duration of the New Horizons

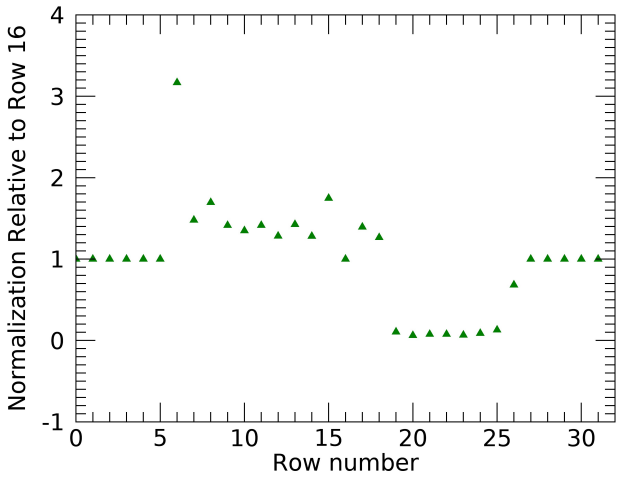

Figure 4. Normalization factor applied to each row to account for relative sensitivity to diffuse/extended sources compared with that in Row 16, which has been extensively calibrated, using a 3600 s dark sky observation. Detector rows 0–5 and 27–31 are outside of the FOV of the slit and are therefore set to 1. The normalization array shown in this figure is applied to each row in the scan observations to calculate the Lyα flux across the Alice FOV.

mission against UV-bright stars (S. A. Stern et al. 2008). We then apply those same normalization values to each row in the data collected during the high-resolution scans.

3.4. Starlight Contamination

Most stars are not a significant source of Lyα emission in the sky because hot stars exhibit a strong stellar absorption line and cool stars have relatively weak chromospheric emission lines. However, hot stars do contribute significantly at other UV wavelengths, and therefore must be removed from parts of our analysis. To identify pixels that may be contaminated with starlight, we set a detection threshold above the observed background, which is typically $\sim$0.05 photons s^{-1} cm^2. If we detect a flux higher than 0.25 photons s^{-1} cm^2 at wavelengths longer than Lyα, then this indicates that there is likley a star. We use the average of the signal between 1550 Å and 1600 Å to flag possible starlight contamination. In some cases, such as hot white dwarfs, the spectrum peaks at wavelengths shorter than Lyα. To identify possible contamination from those objects, we average the signal in each pixel between 920 and 970 Å and flag a possible star if the signal is $>$0.1 photons s^{-1} cm^2. We baseline these criteria through visual inspection of how well they identify data with stars without given false positives. Depending on the analysis, we either removed the stars from the dataset or we simply flagged pixel locations to better interpret any deviations in observed flux variation (see Section 4). We also compare such flux variations potentially caused by astrophysical objects by plotting the entire Alice map and overplotting the position of the stars using the Catalog of Ultraviolet Bright Stars (CUBS) by M. A. Velez et al. (2024). See Section 4 for these final plots and star locations within the high-resolution UV and Lyα maps.

4. Results

The high-resolution Lyα scans reveal a modest amount of variability of Lyα emissions, ranging between 111 R $-$160 R, with an average signal of 138 R, or a range of 72–105 photons $s^{-1}cm^{-2}$ with a mean value of 90 photons s^{-1} cm^{-2}. One R is equal to 10^6 photons s^{-1} cm^{-2} $(4\pi$ sr$)^{-1}$. We compare this with the broader UV bandpass from 700 to 1800 Å and find the range in UV signal to be from 127 R to 205 R, with an average intensity of 151 R, or from 83 to 134 photons $s^{-1}cm^{-2}$ with an average intensity of 99 photons s^{-1} cm^{-2}. The average error in the data for both the Lyα and the full UV bandpass is between 10 and 15 R.

We present maps of the high-resolution scans at Lyα wavelengths (Figure 5) and of the full UV bandpass (Figure 6). To produce these maps we discretize the region into $0.^{\circ}05 \times 0.^{\circ}5$ spatial bins and assign each descretized point a brightness value based on the Alice pixels that cover that location. The size of the patch observed by a single Alice row is shown as overlapping white and yellow boxes near Galactic longitude and latitude of 305° and $-81.^{\circ}5$. These boxes represent the effective FOV size of Row 9 over one integration period in the first scan and its overlapping position over a single integration during the second scan. The discretized points that make up the map sample from different Alice rows during the two scans; the maps show the average brightness measured in a given spatial location.

The maps show that within the larger Alice FOV box, the brightness is more uniform; this results from each row in the box viewing a much broader instrument FOV solid angle of sky. This builds a higher signal-to-noise ratio (SNR) at the expense of spatial resolution. In the region sampled by the narrower Alice slot, spatial variability is more easily detected. There appear to be a few "hot spots" in both the Lyα map, Figure 5, and in the UV brightness map in Figure 6. The map shows the locations of stars to identify any correlation in brightness variation, as discussed in more detail in Section 4.2.

4.1. Implications for Alice Global Map of Lyα

We first compare our average Lyα brightness with an observation from the deep-sky Alice observation campaign designed to retrieve the cosmic UV background (J. Murthy et al. 2025). The FOV of observation NCOB06 from that campaign centered the boresight on average near R. A. $= 9.^{\circ}46455$, decl. $= -32.^{\circ}73273$ or Galactic longitude and latitude $(l, b) = (329.^{\circ}798, -83.^{\circ}671)$ and is within the region observed with the Lyα scans reported here. The deep-sky observation was conducted for 3600 s and the resulting observed Lyα brightness was 136.5 $\pm$ 4.7 R. In that region, the Lyα scans in this analysis show a brightness of $\sim$136.6 $\pm$ 0.9 R, demonstrating that even deeper stares with higher SNR are consistent with our findings.

One of the goals of the high-resolution Lyα scan observations was to conduct the same experiment as the observations that produced the global Lyα presented in G. R. Gladstone et al. (2025), but in this case to obtain spectral information so that Lyα could be isolated from the rest of the spectral bandpass. These data were also acquired in a region with few UV-bright stars and using longer integrations to improve SNR. Figure 7 shows a series of plots: the brightness at Lyα, the brightness in the full Alice UV bandpass, and the ratio of these two values for Row 16 and Row 21. The results indicate that, in the slot, the ratio of Lyα to the full UV bandpass is on the order of 90%, and in the box it is 98%.

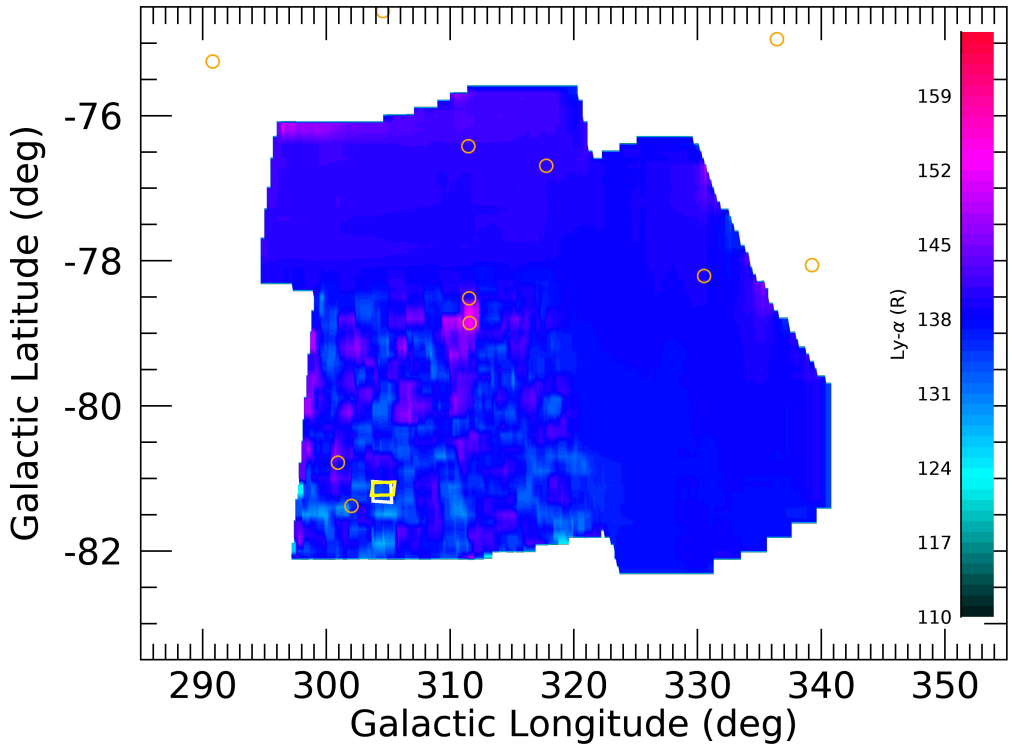

Figure 5. Map of Lyα brightness in R. The map shows some variability in brightness ranging from 110 to 160 R. The more uniform swaths at the top and right are regions observed by the Alice box, which average over a much larger region with each step of the instrument than the higher resolution region produced by the narrow $0.^{\circ}1$ slot. The orange circles represent locations of UV-bright stars listed in the CUBS catalog (M. A. Velez et al. 2024). The overlapping white and yellow boxes near 305° longitude are the outlines of Row 9 over one integration period during each of the two scans. The overlapping region provides an indication of the effective spatial resolution of our map.

We then mimic the way the global maps were produced by summing the photon counts over the entire FOV without any row normalization (Section 3.3). The ratio of Lyα to all counts within the UV bandpass between 700 and 1800 Å results in a ratio of 96%–97% over the duration of the observations, except when stars are within the FOV (see Figure 8). This could indicate that there may be an overestimate of Lyα up to 4% in the global maps produced by G. R. Gladstone et al. (2025). However, we note that the Lyα values derived from the global maps are more in line with the Lyα values reported in this work. In fact, the global map indicates a range of Lyα brightness between 129.0 and 140.3 R, with an average of 132.8 R. This result suggests that the difference in the brightness between the Lyα data and the full UV bandpass data is noise, which is consistent with the spectra shown in Figure 3. These results indicate that the method used by G. R. Gladstone et al. (2021) to remove stellar signals using the CUBS catalog does a good job of removing background signal.

Because the Lyα signal derived from the spectrally resolved Alice images in the high-resolution scans matches the Lyα signal derived from Alice in photometer mode, future observations by New Horizons could similarly be acquired in photometer mode rather than using the spectral images. This method would allow for a more conservative data volume for the observation sets. Such observations can further be used to characterize any observed changes in the Lyα signal detected as New Horizons continues to travel beyond the outer reaches of our solar system.

4.2. Sources of Observed Structure

4.2.1. Stars and Galaxies

We investigate the hot spots (regions of higher intensity) in both the Lyα and full UV bandpass maps (Figures 5 and 6). We identify the hot spot near $(l, b) = (311^{\circ}, -78.^{\circ}5)$ as λ^1 Sculptoris, which is a binary system with a B9.5V type star and an A9 type star. The Galactic coordinates provided in the SIMBAD system (M. Wenger et al. 2000) for this star system are $(l, b) = (311.^{\circ}54068, -78.^{\circ}51857)$. In Figure 6(B) we show the stellar spectrum in our data, which is consistent with that of a B9 star.

We identify the hot spot in the UV brightness map in Figure 6 near Galactic coordinates $(l, b) = (300^{\circ}, -79.^{\circ}5)$ as NGC 300, also known as the Sculptor Pinwheel Galaxy, which is located at $(l, b) = (299.^{\circ}209, -79.^{\circ}419)$ (I. Platais et al. 1998). As described in the subsequent sections, this object is also detected in the maps produced by the Planck observatory and the GALEX observatory. The galaxy's spectra in Figure (6(D)) appear as a broad enhancement in flux from ~920 Å to ~165 Å. This spiral galaxy has a small redshift ($z = 0.000491$) or relative velocity of 141 km s^{-1}, which is imperceptible with Alice's spectral resolution.

4.2.2. Sources of Structure in Lyα Emission

Spectra taken in the region around the hot spot near $(\ell, b) = (311.^{\circ}6, -78.^{\circ}5)$ are shown in Figure 6(B), consistent with the hot subdwarf sdB CD−38 222. Also named SB 290 (A. Slettebak & R. K. Brundage 1971; J. A. Graham & A. Slettebak 1973), this star has J2000 Galactic coordinates

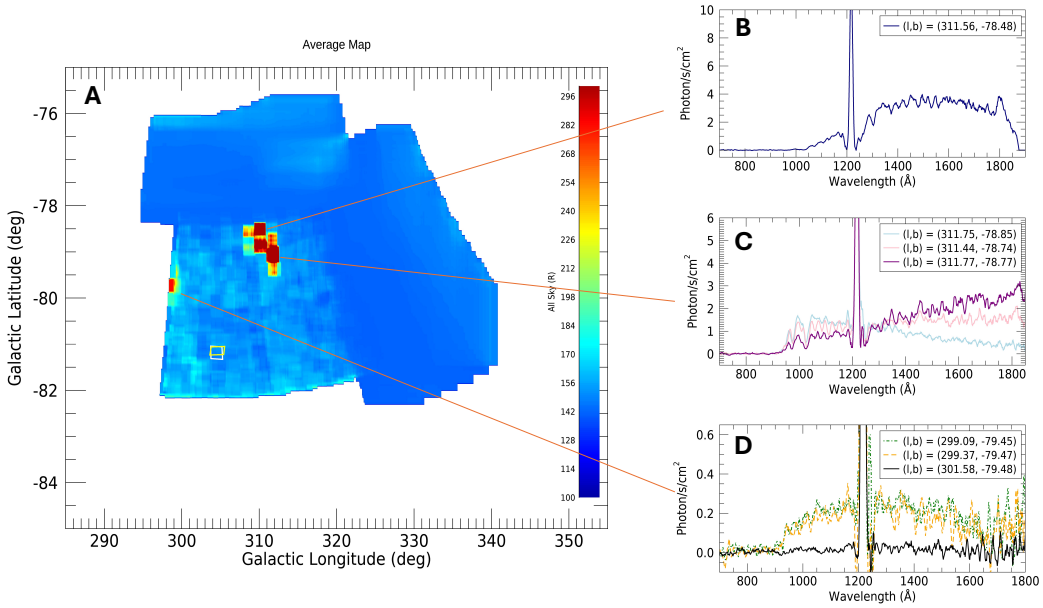

Figure 6. (A) Map of UV brightness integrated from 700 Å to 1800 Å. This figure is the same as Figure 5 apart from integrating over the longer spectral bandpass. We find three regions of "hot pixels" and show the spectra from those regions in the subfigures B–D. (B) The location and spectra of the hot pixel region are consistent with star λ^1 Scl. (C) Spectra from three map pixels centered near the location of the hot subdwarf CD−38 222. (D) Spectra from two map pixels showing a broad but mild increase in signal centered near Lyα. The location is consistent with galaxy NGC 300, also known as the Sculptor Pinwheel Galaxy. Note that the Galactic coordinates provided for each spectrum correspond to the location of the Alice boresight at the midpoint of the integration.

$(\ell, b) = (311.^\circ579256, -78.^\circ858702)$ and magnitudes $B = 10.19 \pm 0.03$ and $V = 10.26 \pm 0.03$ from the Tycho-2 survey (E. Høg et al. 2000). Its Gaia-DR3 parallax distance is 183 ± 5 pc. Therefore, it is located at high Galactic latitude in the direction toward the South Galactic pole, and is approximately 180 pc below the Galactic disk. We confirmed the hot subdwarf location using the Gaia map of such objects produced by R. Culpan et al. (2022). S. Geier et al. (2013) found that SB 290 is a rapidly rotating ($V_{\rm rot} \sin i = 58 \pm 1$ km s^{-1}) hot subdwarf on the extreme horizontal branch with effective temperature $T_{\rm eff} = 26{,}300 \pm 100$ K and surface gravity $\log g = 5.31 \pm 0.01$, parameters derived from their photometry and a grid of line-blanketed, solar metallicity LTE model atmospheres. With an estimated stellar mass $M = 0.6\,M_\odot$, it has a mean radius $R = (GM/g)^{1/2} = 0.284 R_\odot$ and bolometric luminosity $L = 4\pi R^2 \sigma_{\rm SB} T_{\rm eff}^4 = 35\,L_\odot$.

The observed stellar color $(B - V) = -0.07 \pm 0.04$ of SB 290 suggests some reddening from the intervening interstellar medium (ISM). Based on fits to optical and UV spectra, U. Heber et al. (1984) quoted a selective extinction $E(B - V) = 0.025$. L. Danly et al. (1992) quoted $E(B - V) = 0.03$ with an H I column density $\log N_{\rm HI} = 20.41$ ($N_{\rm HI}$ in cm^{-2}) from Lyα absorption measurements taken with the International Ultraviolet Explorer. Typical uncertainties for this technique are ± 0.10 in $\log N_{\rm HI}$. We will adopt $E(B - V) = 0.03 \pm 0.01$, with $N_{\rm HI} = 2.57 \times 10^{20}$ cm^{-2} and using the mean interstellar gas-to-dust ratio, $N_{\rm H}/E(B - V) = 9 \times 10^{21}$ cm^{-2} mag^{-1}, found toward 51 AGN at high Galactic latitudes (J. M. Shull & G. V. Panopoulou 2024).

The hot subdwarf SB 290 appears to be a single high-latitude star, with no sign of any companion. However, it may have formed through a binary merger (S. Geier et al. 2013). The observed increase in flux at longer wavelengths for Row 17 suggests that any undetected companion would be brighter in the visible than the primary object itself and would likely have been detected previously. S. Geier et al. (2013) reported no sign of a cool companion from photometric or radial-velocity variations, including in planetary transit surveys (D. L. Pollacco et al. 2006).

Unlike the other two hot spots, the location of the hot subdwarf CD-38 222 is also coincident with an increase in Lyα observed in Figure 5. Much of this uptick is seen in Row 18, which is a more difficult row to fully calibrate because it is the row where the FOV transitions from the slot/stem to the box. However, we also see a slight increase in Lyα in Row 17, and therefore further investigate the cause. The brightest spot near SB 290 has a residual Lyα surface brightness of 25 R above the 133 R mean background emission averaged over the nearby region. G. R. Gladstone et al. (2025) provide further discussion of these backgrounds. Another stellar Lyα source appearing prominently above background in the New Horizons Lyα scans is the "Spica Nebula," where the Alice spectrograph measured ∼60 R of Lyα emission above background (G. R. Gladstone et al. 2025). Located at high Galactic latitude ($b = 50.^\circ84$), this nebula extends 10°–13° around the B1-star binary α Virginis. Its diffuse Hα emission of 3–5 Rayleighs (D. P. Finkbeiner 2003) may arise from an ionizing source with Lyman-continuum (LyC) photon luminosity $Q_{\rm H} \approx 10^{46.2}$ s^{-1} (J.-W. Park et al. 2010; J. P. Aufdenberg & J. M. Hammill 2021).

These sources of Lyα emission could be nebular emission produced by ionizing photons from the central hot star, or from shock excitation as the star interacts with a high-latitude interstellar gas cloud. Spica has a mean radius $R \approx 7.1 R_\odot$ at estimated mass $M \approx 10 M_\odot$ and surface gravity $\log g = 3.741$ (J. P. Aufdenberg & J. M. Hammill 2021). For an ionized gas sphere around a LyC source with $Q_{\rm H} = (10^{46}\,{\rm s}^{-1}) Q_{46}$ inside a cloud with total hydrogen density $n_{\rm H}$ (in cm^{-3}) and electron

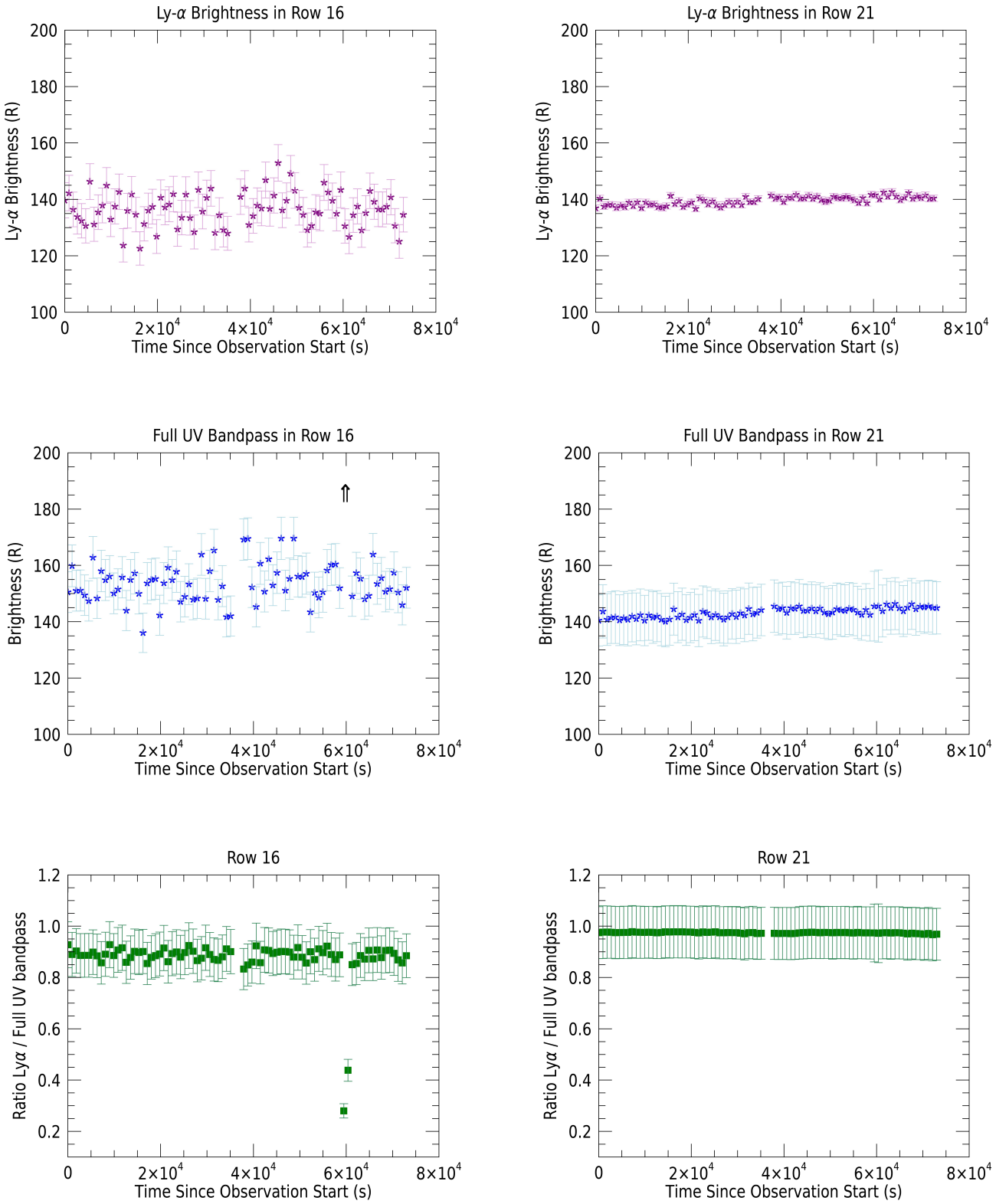

Figure 7. The Lyα brightness and the brightness across the UV bandpass, and the ratio of the two brightnesses as a function of time since the observations started. These plots are for Row 16 in the slot and Row 21 in the box. The arrow in the full UV bandpass for Row 16 indicates two bright points (>500 R) due to a star in the row, which results in the lower Ratio of Lyα to UV bandpass at that same time ($\sim 6 \times 10^4$ s after start). The small gap in data near 2.5×10^4 s after start reflects the time needed to reposition the FOV between the first and second scans.

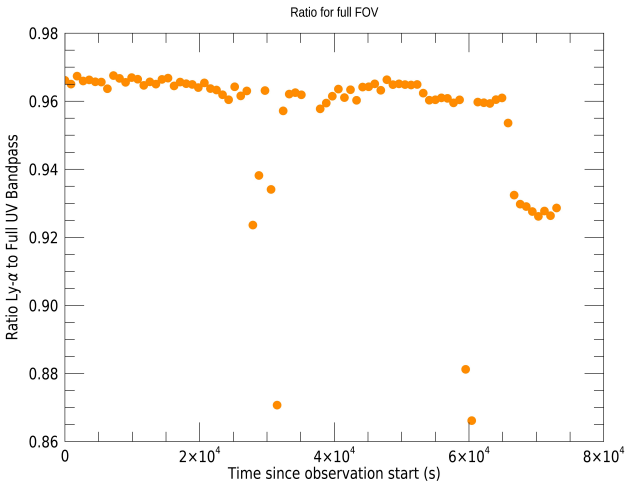

Figure 8. Ratio of the Lyα signal to the full UV bandwidth after summing the signals across the entire Alice FOV. The small gap in data is during the time between the first and second scan. The drops below 95% all occur when stars are present in the FOV. The drop is less pronounced than seen in Figure 7 because an individual star in a single row contributes significantly less when measuring the Lyα signal across the entire detector. The average ratio is between 96% and 97%, supporting the use of the instrument in photometer mode to accurately report on Lyα within 4% without needing to collect the full UV spectrum and isolating the emission line for large-scale maps such as those produced by G. R. Gladstone et al. (2025).

density $n_e = 1.1 n_{\rm H}$, the Strömgren radius is

$$R_s = \left[\frac{3Q_{\rm H}}{4\pi n_e n_{\rm H} \alpha_{\rm H}^{(2)}}\right]^{1/3} \approx (6.58\ {\rm pc}) Q_{46}^{1/3}\, n_{\rm H}^{-2/3}. \quad (1)$$

Here, we adopted $\alpha_{\rm H}^{(2)} = 2.59 \times 10^{-13}\ {\rm cm^{-3}\ s^{-1}}$ as the case B radiative recombination rate coefficient to excited levels ($n \geqslant 2$) at temperature $T \approx 10^4$ K. In equilibrium, each photoionization is balanced by a recombination, with fractions $\epsilon_{\rm Lya} = 0.677$ and $\epsilon_{\rm Ha} = 0.453$ producing Lyα and Hα photons. For pure photoionization, the expected photon flux ratio would be $\epsilon_{\rm Lya}/\epsilon_{\rm Ha} = 1.49$. The Ly$\alpha$ surface brightness from the projected solid angle of the nebula, $(\pi R_s^2/d^2)$ at distance d would then be

$$B({\rm Ly}\alpha) = \frac{0.677 Q_H/4\pi d^2}{\pi R_s^2/d^2} = \left[\frac{5.23 \times 10^6\ {\rm phot\ cm^{-2}\ s^{-1}}}{4\pi\ {\rm ster}}\right] Q_{46}^{1/3}\, n_{\rm H}^{4/3}. \quad (2)$$

The coefficient inside brackets corresponds to a brightness of 5.23 Rayleighs for $n_{\rm H} = 1\ {\rm cm^{-3}}$, consistent with the observed range of Hα in the Spica Nebula. Photoionization models of the nebula around α Vir (D. G. York & B. F. Kinahan 1979; J.-W. Park et al. 2010; J. P. Aufdenberg & J. M. Hammill 2021) found densities $n_e =$ 0.3–0.5 cm^{-3} with $Q_{\rm H} \approx 10^{46.2}\ {\rm s^{-1}}$. However, the large ratio of photon fluxes (Lyα/H$\alpha \approx$ 5–8) in the Spica Nebula is considerably higher than typical values ($\sim$1.5) for case B recombination at $T = 10^4$ K. This ratio may indicate contributions from shock excitation of H I, which preferentially excites Lyα compared to Hα. This discrepant ratio could also arise from contamination of the Lyα signal by scattered far-UV (FUV) starlight from the star, which enters the "all-signal" bandpass (700–1800 Å) of the Lyα scans.

We now consider possible sources of the Lyα emission around the hot subdwarf SB 290, which is much less luminous than Spica. SB 290 has a Gaia-DR3 parallax distance 183 $\pm$ 5 pc, radial velocity $V_{\rm rad} = -52.3 \pm 2.7\ {\rm km\ s^{-1}}$ (G. A. Gontcharov 2006), and transverse velocity $V_{\rm tr} = 39.0 \pm 1.2$ km s^{-1}. This gives SB 290 at high total space velocity, $V_* = 65 \pm 3\ {\rm km\ s^{-1}}$. Relative to the ISM, this velocity is both supersonic and supermagnetosonic, and its passage through an interstellar cloud would likely produce a bow shock (B. E. Wood 2004; J. M. Shull & S. R. Kulkarni 2023). This encounter would produce both an H II region and a bow shock, with Lyα brightness depending on the gas density $n_{\rm H}$ and the filamentary density structure of hydrogen within the cloud. For these high-resolution scans, no other stars within the Alice FOV appear to be affiliated with Lyα enhancements.

The strength of bow-shock Lyα emission depends on the stellar velocity V_* and gas density $n_{\rm H}$. Galactic 3D dust mapping (G. Edenhofer et al. 2024) toward SB 290 shows low extinction along the sight line out to distances $\sim$100 pc from the Sun, owing to the low-density Local Hot Bubble. However, the extinction increases substantially at distances d = 180–210 pc. Thus, SB 290 may have entered an interstellar cloud less than 100,000 yr ago, and a bow shock could be responsible for some of the Lyα emission. In contrast to Spica and its surrounding nebula, the Lyα emission around SB 290 is unlikely to come from its H II region. Scaling the LyC photon luminosity as $Q_{\rm H} \propto R^2 T_{\rm eff}^4$, we estimate that SB 290 has 500 times smaller LyC luminosity than Spica. This reduction follows from the much smaller stellar radius ($0.284 R_\odot$ for SB 290 versus $7.1 R_\odot$ for Spica) despite similar effective temperatures (26,300 K and 24,800 K).

Using the bow-shock formula (Equation (14) in J. M. Shull & S. R. Kulkarni 2023), we estimate a Lyα surface brightness

$$B({\rm Ly}\alpha) \approx (50\ {\rm R}) \left(\frac{V_*}{65\ {\rm km\ s^{-1}}}\right)^{2.25} \left(\frac{n_{\rm H}}{1\ {\rm cm^{-3}}}\right), \quad (3)$$

where we scaled the density of the preshock ISM to $n_{\rm H} = 1\ {\rm cm^{-3}}$. To produce a Ly$\alpha$ brightness of 25 R at 65 km s^{-1} speed, SB 290 would need to pass through an interstellar cloud with density $n_{\rm H} \geqslant 05\ {\rm cm^{-3}}$. In the Galactic plane, densities of this level are common. Because SB 290 lies near the South Galactic pole, 180 pc below the Galactic plane, this density may indicate an interesting interstellar cloud in its immediate vicinity. Follow-up spectroscopic observations could be made along the line of sight to SB 290 to substantiate the presence of interstellar material with a dense filamentary structure surrounding the star.

In the atmosphere of the hot sdB star SB 290 with radial velocity $-53.2\ {\rm km\ s^{-1}}$, the Lyα line would appear in absorption, shifted by 0.22 Å to the blue of 1215.67 Å. The Lyα nebular emission lines will be shifted by diffusive scattering within the Doppler core of the line, undergoing a random walk in frequency space into the line wings. The Lyα lines emerge in the damping wings of the Lyα absorption profile as effectively FUV continuum photons. For the ISM toward SB 290, most of the column density, $N_{\rm HI} \approx 2.6 \times 10^{20}\ {\rm cm^{-2}}$, is farther than 70 pc from the Sun (C. Zucker et al. 2025), owing to the presence of the Local Hot Bubble. The Lyα optical depth at line center is $\tau_0 \approx 10^7$. The scattering Lyα lines emerge in the line wings, shifted in

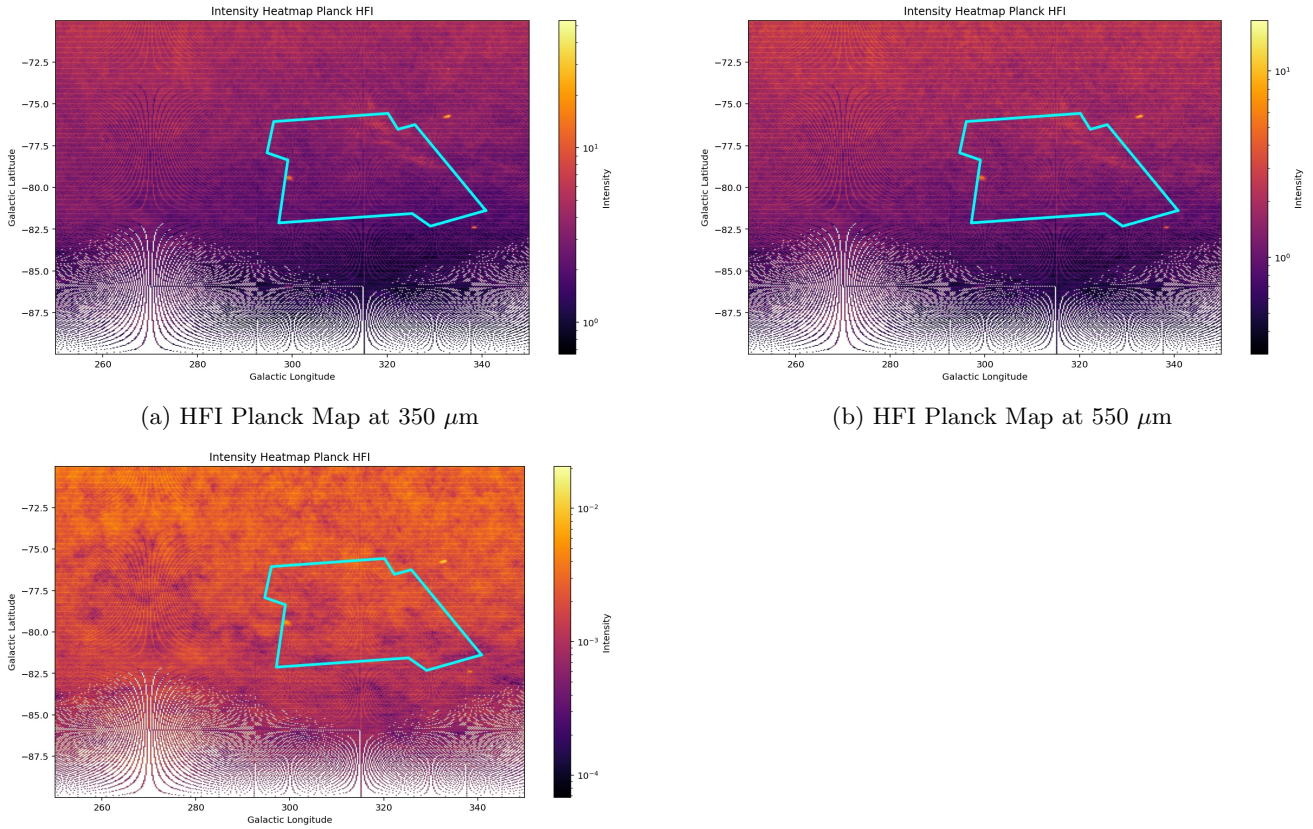

(a) HFI Planck Map at 350 μm

(b) HFI Planck Map at 550 μm

(c) HFI Planck Map at 850 μm

Figure 9. Subset of maps showing variability in observed signal at 350 μm, 550 μm, and 849 μm as observed by HFI on the Planck space observatory in the region of sky where the Lyα scans were made. The units for the Planck observations are $K_{\rm cmb}$ at 550 μm and MJy sr^{-1} at 849 μm. The cyan region outlines the region of space observed during the Alice scans. Some variation in the Planck data is noted in each, particularly at 849 μm. There is also a cloud-like structure most easily seen in the 350 and 550 μm data panels stretching from 315° to 330° in Galactic longitude and −75° to −79° in Galactic latitude.

dimensionless frequency by a factor

$$x_s = \Delta\nu_s/\Delta\nu_D = 13\, N_{20}^{1/3} T_{7000}^{-1/6}. \quad (4)$$

Here, we scaled to H I column density $N_{20} = N_{\rm HI}/10^{20}\,{\rm cm}^{-2}$ and adopted a Doppler frequency,

$$\Delta\nu_D = (b/c)\nu_0 = (8.85 \times 10^{10}\,{\rm Hz})\, T_{7000}^{1/2}, \quad (5)$$

with Doppler velocity parameter $b = (2kT/m_H)^{1/2}$ and ISM temperature $T = (7000\,{\rm K})T_{7000}$. With $N_{20} = 2.6$, we find $x_s \approx 18$, corresponding to a shift in wavelength from line center by $\Delta\lambda_s \approx 0.78$ Å. A fuller discussion of the Lyα scattering process is given in M. Dijkstra (2014) and in Section 4 of G. R. Gladstone et al. (2025).

The dust-to-gas ratio at high Galactic latitudes (H. Liszt 2024; J. M. Shull & G. V. Panopoulou 2024) is considerably lower than in the Galactic plane (B. T. Draine 2011). The FUV extinction in the Lyα wings ($\lambda \approx 1215$ Å) scales with hydrogen column density as

$$A_\lambda \approx (10 \times 10^{-22}\,{\rm cm}^2\,{\rm mag})\, N_{\rm H}. \quad (6)$$

With $\log N_{\rm HI} = 20.41$ toward SB 290, we estimate dust extinction in the Lyα wings of $A_\lambda \approx 0.26$. For dust grains with FUV albedo of 0.5, the expected absorption optical depth should be small ($\tau \approx 0.14$). Therefore, if strong bow-shock emission is formed around SB 290, we find it reasonable that we would see its emission at the level observed in the New Horizons Alice Lyα map.

4.2.3. Planck Maps

We compare the observed variations of Lyα with Planck maps of thermodynamic temperature and surface brightness obtained by the High Frequency Instrument (HFI) on the Planck space observatory operated by the European Space Agency (Planck Collaboration et al. 2011). These parameters generally track the distribution of interstellar dust and we examine them for structures that correlate with UV variations in our maps. Figure 9 shows the Planck data at 350 μm, 550 μm, and 849 μm, with a yellow box marking the region observed by Alice. We note the wispy cloud-like structure stretching from 315° to 330° in Galactic longitude and −75° to −79° in Galactic latitude that could be indicative of a localized bubble. However, this region was observed in the Alice box at lower angular resolution, and we do not see any corresponding features in the Lyα or UV brightness maps.

We sample the high-resolution maps produced by Planck data at 350 μm, 550 μm, and 849 μm (Figure 9) at the resolution of the Alice observations by averaging the Planck signal within the bounds of each Alice row covered in each observational time step. We then compare the signal in these synthetic Planck scans to our Alice scans, examples are plotted in Figure 10 as a function of approximate Galactic latitude and Galactic longitude. We note that the Alice scans were not

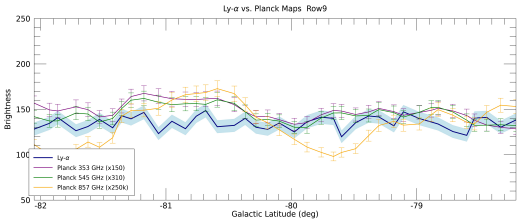

(a) Alice Row 9 Galactic Latitude

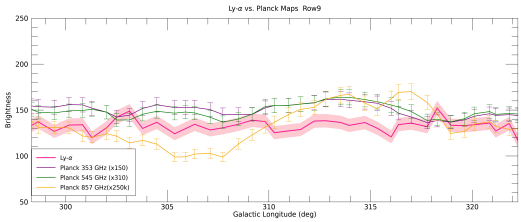

(b) Alice Row 9 Galactic Longitude

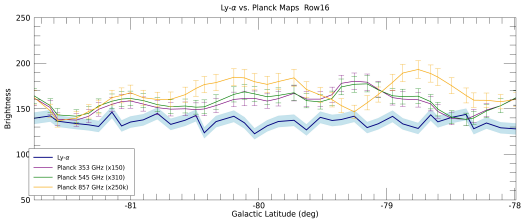

(c) Alice Row 16 Galactic Latitude

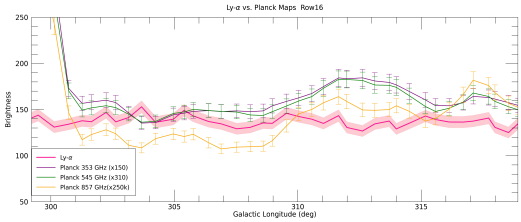

(d) Alice Row 16 Galactic Longitude

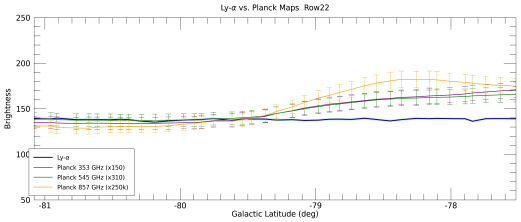

(e) Alice Row 22 Galactic Latitude

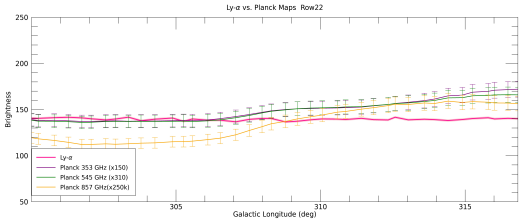

(f) Alice Row 22 Galactic Longitude

Figure 10. Variability of Lyα signal compared with variation in thermodynamic temperature and surface brightness maps produced from data collected by HFI on the Planck space observatory in selected Alice rows. The data shown as a function of Galactic Latitude were acquired during the Alice scan that traversed the sky mostly along Galactic Longitude, but we note that it was not necessarily a constant Galactic longitude. The same is true for the data shown as a function of Galactic longitude. The units for the Planck observations are $K_{\rm cmb}$ at 353 GHz and MJy sr^{-1} at 545 GHz and 857 GHz. The intensity of the Planck data is scaled to match the signal at Lyα wavelengths.

conducted at a constant Galactic latitude or longitude; however, the plots give a sense of how the overall signal changes as a function of position in the sky. The observed signal fluctuations in the box (e.g., Row 22) are smoother because of the much larger region covered by the larger row (Section 3) and the relatively small shift in sampled region with each observational time step.

Figure 10 again shows the relatively constant Lyα signal during each scan, while the Planck data show greater undulations and even sharp peaks at some locations in the sky. We do not find a correlation between the Lyα signal with the variability at longer wavelengths observed in the Planck dataset within the errors. Here, we use the conservative 5% systematic errors on the Planck data determined by Planck Collaboration et al. (2016).

This lack of fine-scale correlation is not surprising given that G. R. Gladstone et al. (2025) concluded that the observed, relatively uniform Lyα signal from the Alice all-sky survey is due to young, hot stars within the Local Bubble that shine on the Bubble's interior walls and photoionize the hydrogen atoms there. This results in a bright, relatively uniform emission of Lyα in all directions within the Local Bubble, whereas variability in the Planck maps trace out the dust distribution across the Galaxy at larger distances than the walls of the Local Bubble (M. Postman et al. 2024). This may indicate that the dust within the Local Bubble is not obscuring much of the Lyα.

More broadly, the Planck maps show a steady decrease in brightness with increasing Galactic latitudes. The Lyα map appears to show the same trend, with slightly dimmer pixels at the higher latitudes and most of the hot spots located at lower latitudes. This observation would suggest that as the dust decreases, so does the Lyα emissions, which would not be expected. This pattern should be more thoroughly explored at other locations in the Galaxy.

We also compare our findings with GALEX mission maps (D. C. Martin et al. 2005; P. Morrissey et al. 2005). J. Murthy (2014) extracted the diffuse background from the GALEX data in the FUV (1350–1780 Å) and near-UV (NUV; 1770–2730 Å). These data are shown in Figure 11, with an outline in magenta indicating the overlapping region observed in the high-resolution Lyα scans. The GALEX data used in this paper can be found on the MAST archive (http://archive.stsci.edu/prepds/uv-bkgd/).

The GALEX data are incomplete in this region due to the avoidance of bright UV stars and much of the Alice region was not imaged by GALEX; however, there are two key takeaways gleaned by comparing the portions of our maps in common. The first is that, like the Alice observations, the GALEX observations in this region do not vary significantly. The second is that the primary deviation from a relatively constant

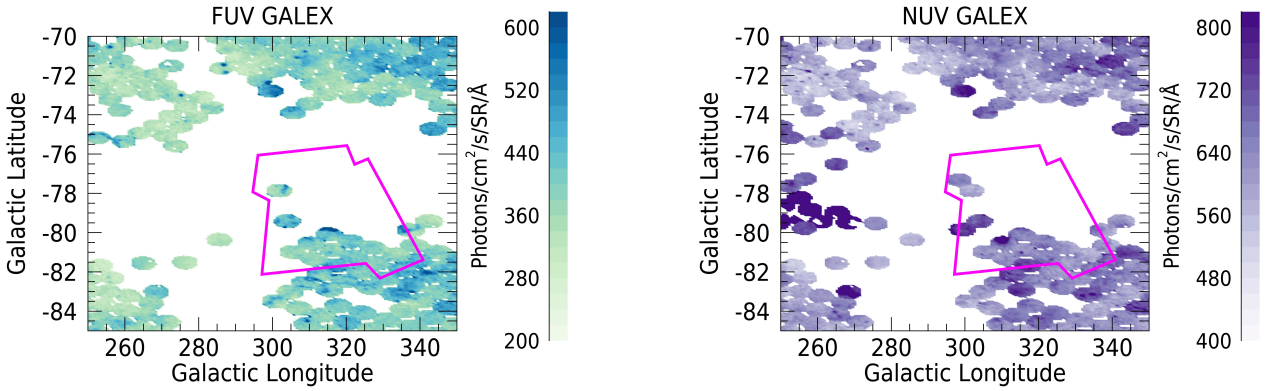

(a) FUV GALEX Map (b) NUV GALEX Map

Figure 11. GALEX Maps shows the FUV and NUV brightness. The magenta shape represents the general region where the Alice data were acquired.

brightness is that the one brighter (>800 photons s^{-1} cm^{-2} SR^{-1} Å) data point in the NUV data that falls within the New Horizons Alice FOV located near (l, b) = (300°, −80°) is coincident with the observed Alice FUV increase near the galaxy NGC 300 Section 4.2.1.

5. Conclusions

We present high angular resolution New Horizons Alice observations of interstellar Lyα emissions from a vantage point of 57 au from the Sun. From this heliocentric distance, our dataset avoids much of the backscattered solar Lyα concentrated in the inner solar system. The scans, orthogonal to one another, were designed to produce a higher SNR, higher spatial resolution map of a small, dark region of space to be compared with the global ν maps produced by G. R. Gladstone et al. (2025). These Alice observations were conducted in a mode that captured the spectral information so that we could isolate the Lyα signal from the rest of the UV bandpass, in contrast to the global sky maps that attributed all photon counts as H Lyα since the emissions from hydrogen are expected to dominate the sky compared to the rest of the UV bandpass. We confirm that this assumption is valid within 4% of the total counts, which is within the error stated by G. R. Gladstone et al. (2025).

Similarly to the larger scale global map, we find the average background Lyα signal to range between 111 R and 160 R, with an average signal of 138 R, and we report very little variation or structure in the Lyα emission and a similar lack of correlation with maps at other wavelengths. This conclusion supports the hypothesis put forth by G. R. Gladstone et al. (2025) that the observed Lyα signal is primarily produced within our Local Bubble.

We identify a slight enhancement (∼25 R) in Lyα over the background signal near the hot sub dwarf CD-38 222, which we calculate to be consistent with emission from a bow shock created as the relatively fast-moving object moves into a region of neutral hydrogen, though we note that this is only one possible explanation for the enhancement in Lyα emissions.

We compared the New Horizons Alice observations with GALEX and Planck observations of the same region. While there appears to be a gradual change in the intensity of the signal in Planck data, the GALEX and Alice data do not appear to have broad brightness trends. All three missions clearly detect the Scultpor Pinwheel Galaxy, as seen in Figure 6.

Future follow-up observations could focus on other stellar objects with high velocities to search for similar Lyα excess, potentially related to bow shocks arising from the interaction of their astrospheres with interstellar neutrals. Additional high-resolution Alice scans obtained in other regions of the sky would enable more searches for subtle sky brightness variability in both the UV background and in H Lyα.

Acknowledgments

We thank Jeffrey Linsky for his review of this manuscript that resulted in a more thorough discussion of the implications of the Alice observations. We acknowledge the New Horizons team for acquisition of this data. This work was completed using internal research funding provided by the Southwest Research Institute.

ORCID iDs

Tracy M. Becker https://orcid.org/0000-0002-1559-5954
G. Randall Gladstone https://orcid.org/0000-0003-0060-072X
Joel Wm. Parker https://orcid.org/0000-0002-3672-0603
J. Michael Shull https://orcid.org/0000-0002-4594-9936
Seth Redfield https://orcid.org/0000-0003-3786-3486
Sarah Ruetschle https://orcid.org/0009-0009-4719-263X
Nathaniel J. Cunningham https://orcid.org/0000-0002-8957-7310
Cynthia S. Froning https://orcid.org/0000-0001-8499-2892
Joshua A. Kammer https://orcid.org/0000-0002-3441-3757
John R. Spencer https://orcid.org/0000-0003-4452-8109
Marc Postman https://orcid.org/0000-0002-9365-7989
Tod R. Lauer https://orcid.org/0000-0003-3234-7247
Jayant Murthy https://orcid.org/0000-0003-4034-5137
Maarten H. Versteeg https://orcid.org/0000-0002-2503-9492
Kurt D. Retherford https://orcid.org/0000-0001-9470-150X
Anne J. Verbiscer https://orcid.org/0000-0002-3323-9304
Pontus C. Brandt https://orcid.org/0000-0002-4644-0306
Kelsi N. Singer https://orcid.org/0000-0003-3045-8445
S. Alan Stern https://orcid.org/0000-0001-5018-7537

References

Aufdenberg, J. P., & Hammill, J. M. 2021, ApJ, 923, 10
Culpan, R., Geier, S., Reindl, N., et al. 2022, A&A, 662, A40
Danly, L., Lockman, F. J., Meade, M. R., & Savage, B. D. 1992, ApJS, 81, 125
Dijkstra, M. 2014, PASA, 31, e040
Draine, B. T. 2011, Physics of the Interstellar and Intergalactic Medium, Princeton Series in Astrophysics (Princeton Univ. Press)
Edenhofer, G., Zucker, C., Frank, P., et al. 2024, A&A, 685, A82
Finkbeiner, D. P. 2003, ApJS, 146, 407
Geier, S., Heber, U., Heuser, C., et al. 2013, A&A, 551, L4
Gladstone, G. R., Pryor, W. R., Hall, D. T., et al. 2021, AJ, 162, 241
Gladstone, G. R., Shull, J. M., Pryor, W. R., et al. 2025, AJ, 169, 275
Gontcharov, G. A. 2006, AstL, 32, 759
Graham, J. A., & Slettebak, A. 1973, AJ, 78, 295
Heber, U., Hunger, K., Jonas, G., & Kudritzki, R. P. 1984, A&A, 130, 119
Høg, E., Fabricius, C., Makarov, V. V., et al. 2000, A&A, 355, L27
Lallement, R., Quémerais, E., Bertaux, J.-L., Sandel, B. R., & Izmodenov, V. 2011, Sci, 334, 1665
Liszt, H. 2024, ApJ, 973, 43
Martin, D. C., Fanson, J., Schiminovich, D., et al. 2005, ApJL, 619, L1
Meier, R. R. 1991, SSRv, 58, 1
Meier, R. R., Carruthers, G. R., Page, T. L., & Levasseur-Regourd, A. C. 1977, JGR, 82, 737
Morrissey, P., Schiminovich, D., Barlow, T. A., et al. 2005, ApJL, 619, L7
Murthy, J. 2014, ApJS, 213, 32
Murthy, J., Shull, J. M., Postman, M., et al. 2025, AJ, 169, 103
Park, J.-W., Min, K.-W., Seon, K.-I., Han, W., & Edelstein, J. 2010, ApJ, 719, 1964
Planck Collaboration, Adam, R., Ade, P. A. R., et al. 2016, A&A, 594, A8
Planck Collaboration, Ade, P. A. R., Aghanim, N., et al. 2011, A&A, 536, A1
Platais, I., Girard, T. M., Kozhurina-Platais, V., et al. 1998, AJ, 116, 2556
Pollacco, D. L., Skillen, I., Collier Cameron, A., et al. 2006, PASP, 118, 1407
Postman, M., Lauer, T. R., Parker, J. W., et al. 2024, ApJ, 972, 95
Redfield, S. 2009, SSRv, 143, 323
Redfield, S., & Linsky, J. L. 2015, ApJ, 812, 125
Shull, J. M., & Kulkarni, S. R. 2023, ApJ, 951, 35
Shull, J. M., & Panopoulou, G. V. 2024, ApJ, 961, 204
Siegmund, O. H. W., Stock, J., Raffanti, R., Marsh, D., & Lampton, M. 1993, in UV and X-Ray Spectroscopy of Astrophysical and Laboratory Plasmas: Proceedings from the Tenth International Colloquium, ed. E. H. Silver & S. M. Kahn (Cambridge Univ. Press), 383
Slettebak, A., & Brundage, R. K. 1971, AJ, 76, 338
Steffl, A. J., Young, L. A., Strobel, D. F., et al. 2020, AJ, 159, 274
Stern, S. A., Slater, D. C., Scherrer, J., et al. 2008, SSRv, 140, 155
Velez, M. A., Retherford, K. D., Hue, V., et al. 2024, PSJ, 5, 93
Wenger, M., Ochsenbein, F., Egret, D., et al. 2000, A&AS, 143, 9
Wood, B. E. 2004, LRSP, 1, 2
York, D. G., & Kinahan, B. F. 1979, ApJ, 228, 127
Zucker, C., Redfield, S., Starecheski, S., Konietzka, R., & Linsky, J. L. 2025, ApJ, 986, 58